JCTC Journal of Chemical Theory and Computation

Computational Investigation of Wave Packet Scattering in the Complex Plane: Propagation on a Grid

Robert E. Wyatt and Brad A. Rowland*

Department of Chemistry and Biochemistry, University of Texas, Austin, Texas 78712

Abstract: The time-dependent scattering of a wave packet from a Gaussian barrier is investigated computationally in the complex z-plane. The initial wave packet and the potential energy are obtained through analytic continuation from functions specified on the real-axis. The wave packet is then propagated on the two-dimensional grid. For a low initial wave packet energy, the time evolution is followed by plotting the following functions: $|\psi(z,t)|$, $real(\psi(z,t))$, and the quantum momentum function (QMF), $p(z,t)$. In the reflected packet, an important role is played by ripples (quasi-nodes) forming above the real axis. As these quasi-nodes move down across the real axis, they are 'detected' as 'interference oscillations' in the density. In contrast, the component of the packet below the real axis makes a significant contribution to the transmitted packet. Vector maps of the QMF show hyperbolic flow around quasi-nodes and counterclockwise circular flow around transient stagnation points, where the QMF vanishes. However, when the Pólya vector field (defined by $P(z,t) = p^*(z,t)$) is plotted, circular counterclockwise flow is obtained near the quasi-nodes. The real and imaginary parts of the quantum action function $S(z,t)$ are plotted and the vorticity, defined by the curl of the Pólya field, is used to pinpoint regions of nonanalyticity in the QMF.

1. Introduction

The scattering of a wave packet from a barrier in one-dimension has been investigated computationally since the mid-1960s. Excellent examples are shown in the animations accompanying the book *Visual Quantum Mechanics*.[1] In studies of this type, the single coordinate (x) is invariably real-valued. In what may seem a bizarre extension, in the present study this coordinate will be replaced by the complex coordinate z, and analysis will be performed on the 'extended' 2D scattering problem in the complex plane. The outcome will be that an observer confined to the real axis will detect only a fraction of the rich dynamics ensuing in the complex plane. However, before getting to this, we need to address the following question: Why study quantum dynamics in the complex plane.

The current investigation was motivated by recent studies using approximate *complex-valued quantum trajectories* to solve the time-dependent Schrodinger equation for barrier scattering problems. Complex-valued *classical trajectories* were introduced in the early years of quantum mechanics to deal with the turning point connection problem in WKB theory,[2,3] and in the early 1970s, trajectories of this type were used for classically forbidden processes.[4−8] In 1987, Huber and Heller[9] generalized the real-space version of Gaussian wave packet dynamics[10] to allow for the propagation of complex-valued classical trajectories. An alternative WKB-type formulation employing complex classical trajectories has also been described.[11]

When it comes to complex *quantum* trajectories, the developments are much more recent. These trajectories provide a method for solving the quantum Hamilton-Jacobi equation (QHJE), which is obtained from the Schrodinger equation through use of the ansatz, $\psi(x,t) = \exp[iS(x,t)/\hbar]$ (see the text by Tannor[12]). The complex action function, $S(x,t)$, is the solution to the QHJE. With the guidance condition, $p(x,t) = \partial S(x,t)/\partial x$, and the dynamical equation $dx(t)/dt = p(x,t)/m$, we are led to trajectories with *complex values* for both x and p (the time remains real-valued).

With the restriction that the wave function is known in advance, it is very informative to analyze and plot complex

* Corresponding author e-mail: barowland@gmail.com.

quantum trajectories. Over the past six years, for the *stationary state* case, quantum trajectories have been analyzed and plotted for bound state and scattering problems.[13−19] A detailed analysis of complex quantum trajectories for several one-dimensional stationary state scattering problems has recently been presented.[20,21] In addition, quantum trajectories have recently been analyzed for several *nonstationary* problems.[20,22]

For *nonstationary problems* where the wave function is *not known* in advance, there have been significant developments[23−31] on the use of *real-valued quantum trajectories* for solving the QHJE. In contrast to these developments concerning real-valued quantum trajectories, the use of *complex valued quantum trajectories* for solving the QHJE is at an earlier stage of development. In 2006, Tannor and co-workers derived equations of motion for approximate quantum trajectories evolving in complex phase space.[32] (Interesting commentary on this work has been presented.[33,34]) This method was applied to the one-dimensional scattering of a wave packet from an Eckart barrier,[32,35] and it has been used to describe interference oscillations in the reflected wave packet and to deal with the node problem.[36,37]

In order to enhance our understanding of quantum dynamics in the complex plane, we will study the scattering of an initial Gaussian wave packet from a complex potential surface on a two-dimensional computational grid. Prior to this work, the exact dynamics of wave packet barrier scattering has not been studied in the complex plane. Some new physical results will arise in this and the following paper, which deals with the dynamics of exact quantum trajectories. Some of these new results include the formation of transport of a string of quasi-nodes away from the barrier region, the twisting of trajectories launched from different initial positions around stagnation curves that form between the quasinodes, and the twisting of Pólya vectors around these quasinodes. Understanding the exact dynamics may lead to improved methods for propagating approximate quantum trajectories, especially for the reflected wave packet.

The computational strategy mentioned above appears problematic because the amplitude of the wave function becomes very large even for small departures from the real axis. In order to mitigate the effect of these large values, it is necessary to periodically damp the wave packet near the edges of the grid. This approach leads to stable and reproducible results within a subspace of the computational grid termed the 'viewing window'. The resulting dynamics is then followed by plotting, for a number of time steps, the real part of the wave function and vector maps of the quantum momentum function (QMF). This function is defined by

$$p(z,t) = \frac{\hbar}{i} \frac{1}{\psi(z,t)} \frac{\partial \psi(z,t)}{\partial z} \qquad (1)$$

Interesting dynamical features are revealed when this complex function is plotted as a set of vectors, $\vec{p}(z,t) = [p_r(z,t), p_i(z,t)]$, emanating from points in the complex plane. The imaginary component of this vector is responsible for 'vertical' transport orthogonal to the real axis. Two special points are of interest: poles in the QMF occur at *nodes* where

$\psi(z,t) = 0$, and the QMF becomes zero at *stagnation points* where $d\psi(z,t)/dz = 0$ (and $\psi(z,t) \neq 0$). In addition, for the barrier scattering problem described in this study, the QMF exhibits *hyperbolic flow* around quasi-nodes in the density[21] (these are local minima where the amplitude becomes small but does not reach zero). In order to analyze this flow, the Pólya vector field is introduced,[38−40] and maps of this field show circular counterclockwise flow around quasi-nodes and hyperbolic flow around stagnation points. In addition to these fields, the vorticity of the Pólya field will be shown for the reflected wave packet.

The remainder of this study is organized as follows. The scattering problem and the computational grid are set up in section 2, and computational aspects are discussed in section 3. Plots illustrating wave packet evolution in the complex plane are presented in section 4. Maps showing the quantum momentum field are described in section 5, and properties of the Pólya vector field (including the vorticity) are presented in section 6. The real and imaginary parts of the quantum action function are described in section 7. Finally, a summary appears in section 8.

2. Scattering Problem and Computational Grid

The initial wave packet in the complex plane is obtained through analytic continuation of a Gaussian defined on the real axis. The resulting complex function is

$$\psi(z) = Ne^{-\beta(z - z_0)^2} e^{ik_0(z-z_0)} \qquad (2)$$

where the initial translational energy is $E = \hbar^2 k_0^2/(2m)$. This function is centered at the point $z_0 = (x_0,0)$ and is normalized *only* for integration along the real axis. The normalization factor is $N = (2\beta/\pi)^{1/4}$. The complex-valued Gaussian barrier, centered on the real axis at the point $z_b = (x_b,0)$, is given by

$$V_G(z) = V_0 e^{-\gamma(z - z_b)^2} \qquad (3)$$

Both $\psi(z)$ and $V_G(z)$ possess essential singularities when $y \rightarrow \pm \infty$.

Both $\psi(z)$ and $V_G(z)$ have very large magnitudes for points off the real axis, and this presents a significant challenge for the computational investigation of wave packet scattering in the complex plane. (To illustrate how bad the situation is, let $\beta = 6$ in eq 2. Then, for points fairly close to the real axis, for example $z = (x_0, \pm 3)$, the Gaussian function $\exp(-\beta z^2)$ has about the same magnitude as Avogadro's number!) We will assume that the dynamics relatively close to the real axis is of paramount concern. So, in order to propagate the wave packet on a relatively small two-dimensional computational grid, the packet will be damped or absorbed near the boundaries. However, even if the *initial* packet is damped, the propagated packet will eventually scatter from the boundaries at later times. For this reason, at later times, damping functions and absorbing potentials will be utilized.

In order to implement this procedure, damping functions are introduced near all four boundaries of the 2D computational grid. First, the damping kernel along the x coordinate, for example, is defined by

Propagation on a Grid

J. Chem. Theory Comput., Vol. 5, No. 3, 2009 **445**

$$d(a, b; x) = [1 + \tanh(a(x - b))]/2 \quad (4)$$

This function takes the following limits:

$$d \to 0 \text{ for } x \ll b$$
$$d \to 1 \text{ for } x \gg b$$
$$\text{and } d \to 1/2 \text{ for } x = b$$

In addition, with a sign change for a, the function $d(-a, b; x)$ takes the following limits:

$$d \to 1 \text{ for } x \ll b$$
$$d \to 0 \text{ for } x \gg b$$

The product of the two functions $d(a, b_1; x)$ and $d(-a, b_2; x)$ (for $b_1 < b_2$) gives a box function with rounded edges for which the value is essentially zero except when $b_1 < x < b_2$. In the latter region, this function takes the value unity. Raising this function to a (positive) power then gives a function which damps to zero very rapidly outside of the 'internal' region between b_1 and b_2. This function is defined by

$$D(a, n, b_1, b_2; x) = [d(a, b_1; x)d(-a, b_2; x)]^n \quad (5)$$

For brevity, this function will be denoted $D(x)$. The parameters a and n can be used to control how rapidly $D(x)$ drops to zero.

Since both $\psi(z)$ and $V_G(z)$ become very large away from the real axis, each function was multiplied by damping functions along the y coordinate prior to the time propagation. As a result, the damped initial wave function and potential are given by

$$\psi_D(z) = D(y) \cdot \psi(z)$$
$$V_D(z) = D(y) \cdot V_G(z) \quad (6)$$

Damping was not applied in the x direction since these two functions are relatively localized in this direction.

As the wave packet advances in time, parts of it will eventually scatter from the edges of the computational grid. In order to confine the wave packet and prevent edge reflection at later times, two approaches were used. The first method is to repeatedly damp the wave function near the four boundaries of the grid. For this purpose, a two-dimensional damping function was applied every M time steps. This damping function is defined as product of the one-dimensional damping functions, $D(x)D(y)$.

Another approach may also be used to confine the spreading wave packet and prevent edge reflections. For this purpose, negative imaginary absorbing potentials[41,42] are introduced. In this case, most of the amplitude entering boundary regions near the edges of the grid is absorbed, although some edge reflection is hard to avoid. The damping functions defined earlier can be used to construct the absorbing potentials. We first note that the function $(1 - D(x))$ gives a 'well' with rounded edges. Within the internal region ($b_1 < x < b_2$), this function is zero, and outside of this region it takes on the value one. Along the x coordinate, the absorbing potential, a negative imaginary function, is then

$$V_{abs}(x) = -iV_{ax}(1 - D(x)) \quad (7)$$

where the parameter V_{ax} controls the strength of the absorber. The total potential on the computational grid is then the sum
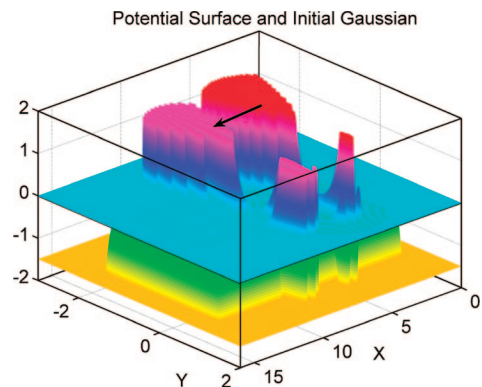
Figure 1. The real part of the (damped) initial Gaussian wave packet (marked with an arrow directed toward the barrier) and the imaginary part of the total potential energy. The initial wave packet energy is $E = V_0/4$. The total potential includes both the Gaussian barrier (damped along the y-coordinate) and the absorbing potential, which is evident near the edges of the computational grid. For viewing purposes, the negative imaginary absorbing potential has been cut off at the lower limit $-1.5i$. (The scaled Gaussian potential is plotted, $V_{sc}(z) = (25/V_0)V_D(z)$).

of the damped Gaussian potential in eq 6 added to absorbing potentials along the x and y directions:

$$V(z) = V_D(z) - iV_{ax}(1 - D(x)) - iV_{ay}(1 - D(y)) \quad (8)$$

Parameter values will now be specified (all values are in atomic units). First, the computational grid extends from $x_{min} = 0$ to $x_{max} = 16$ and from $y_{min} = -3$ to $y_{max} = 2$. There are $N_x = 351$ and $N_y = 251$ grid points along the two coordinates. The initial wave packet is centered at $z_0 = (6,0)$, the width parameter is $\beta = 6$, and the mass is $m = 2000$. The damping parameters used for this function are $a = 10$, $b_1 = -1.7$, $b_2 = 1.4$, and $n = 6$. The barrier is centered at $z_b = (9,0)$, the width parameter is $\gamma = 4$, and $V_0 = 0.035$. The damping parameters used for the potential are $a = 6$, $b_1 = -2.2$, $b_2 = 1.4$, and $n = 6$. The absorbing potential parameters are $V_{ax} = 5$ and $V_{ay} = 1$. The parameters for the $D(x)$ damping function are $a = 10$, $b_1 = 1$, $b_2 = 15$, and $n = 6$. Parameter values (except those specifying the initial wave packet and the Gaussian potential) were determined through experimentation, the goal being to obtain reproducible and accurate values for the scattering wave function at relatively late times ($t \leq 1400$) within a *viewing window* (see below).

Figure 1 shows the real part of the (damped) initial Gaussian wave packet (marked with an arrow directed toward the barrier) and the imaginary part of the total potential energy. The initial wave packet energy is $E = V_0/4$. The pure imaginary absorbing potential is evident from the deep wells near all four edges of the computational grid. For viewing purposes, upper and lower cutoff values were applied to both the wave packet and the potential energy. In order to provide more resolution in the following figures, the results (wave function and quantum momentum) were plotted in a viewing window which is smaller than the computational grid. The size of this window will be evident from the range of the axes in the figures.

3. Computational Aspects

Three explicit time-integration algorithms were utilized for propagating the wave packet in the complex space. The first of these, the forward Euler method (first-order accuracy in Δt, the time step), is given by[43]

$$\psi(z, t + \Delta t) = \psi(z, t) - \Delta t \cdot (i/\hbar)\hat{H}\psi(z, t) \qquad (9)$$

where $\hat{H}$ is the Hamilton operator. For this algorithm, the absorbing potential in eq 8 was used to deal with reflection from the edges of the grid. The second propagation algorithm, the leapfrog method (second-order accuracy), is given by[43]

$$\psi(z, t + \Delta t) = \psi(z, t - \Delta t) - 2\Delta t \cdot (i/\hbar)\hat{H}\psi(z, t) \quad (10)$$

For this algorithm, the damping potential $D(x)D(y)$ was applied to the current wave function after every $M = 20$ time steps. Finally, a version of the Verlet method[44] (fourth-order accuracy) for wave function propagation was used. This algorithm is given by

$$\psi(z, t + \Delta t) = 2\psi(z, t) - \psi(z, t - \Delta t) - (\Delta t/\hbar)^2\hat{H}(\hat{H}\psi(z, t)) \qquad (11)$$

For this case, in common with the leapfrog method, the damping potential was applied to the current wave function every $M = 20$ time steps.

For some of the computations described later, the leapfrog method was used, with the time step in the range $\Delta t = 0.5-1$. Other calculations were run using the Euler method, with a smaller time step in the range $\Delta t = 0.1-0.5$. Calculations were also run using the Verlet method, with a time step in the range $\Delta t = 1-3$. Within the viewing window mentioned earlier, results obtained using these three algorithms agreed very well with each other.

In order to operate with the Hamiltonian on the wave function, we need to evaluate $\partial^2\psi(z)/\partial z^2$. Assuming analyticity of the wave function on the computational grid, this was done by taking the derivative with respect to x: $\partial^2\psi(z)/\partial x^2$. The quantity $\partial^2\psi(z)/\partial z^2$ can also be obtained by taking the y derivative: $-\partial^2\psi(z)/\partial y^2$. As a result, it can be verified numerically that Laplace's equation[39] is satisfied: $\partial^2\psi(z)/\partial x^2 + \partial^2\psi(z)/\partial y^2 = 0$.

In order to compute the quantum momentum from the wave function according to eq 1, we need to evaluate $\partial\psi(z)/\partial z$. Again assuming analyticity, this was done by taking the derivative with respect to x: $\partial\psi(z)/\partial x$. The same result for $\partial\psi(z)/\partial z$ can also be obtained by taking the y derivative: $-i\partial\psi(z)/\partial y$. As a result, it can be verified numerically that the Cauchy-Riemann equation[39] is satisfied: $\partial\psi(z)/\partial x = -i\partial\psi(z)/\partial y$.

4. Wave Packet Evolution

The time dependence of the wave packet was studied by plotting $real(\psi(z,t))$ within the viewing window. For six time steps, Figure 2 shows surface plots of this function along with mesh plots of $imag(V(z))$ (see eq 8). In common with maps showing the quantum momentum (section 5), the initial wave packet energy is $E = V_0/4$. Note that the viewing angle is slightly different for each part of this figure.

Part (a) shows the initial wave packet, labeled with an arrow heading toward the barrier. The component of the wave packet at negative values of y at later times makes the dominant contribution to the transmitted wave packet. However, the component of the wave packet at positive values of y makes an important contribution to oscillatory structure in the reflected wave packet. In part (b), for $t = 300$, the leading edge of the wave packet encounters the barrier potential below the real axis. In part (c), for $t = 500$, the leading edge of the packet has penetrated the barrier region for $y < 0.1$. Note that the de Broglie wavelength for the transmitted packet on the left side of the figure is much smaller than for the reflected packet on the opposite side of the figure. Starting with part (d), for $t = 700$, and continuing with part (e), for $t = 1000$, additional amplitude penetrates to the product side of the barrier. In parts (e) and (f), the latter for $t = 1200$, the component of the wave packet above the real axis undergoes reflection from the barrier. It will be seen in the next section that undulations created *above* the real axis are deflected toward the region below the real axis, and as they cross this axis an observer positioned there would record ripples in the density. In the following section, these features will be linked to the time development of the quantum momentum function.

4. Quantum Momentum Maps

The time dependence of the quantum momentum field, $p(z,t)$, can be studied by superimposing vector maps of the QMF on contour plots of the amplitude of the wave function. (If $\psi(x,y,t) = R(x,y,t)\exp(i\phi(x,y,t))$, where R and ϕ are real-valued, then the amplitude is $|\psi(z,t)| = R(z,t)$.) It was decided not to display flux maps (even though they were computed), where $\vec{j} = \rho\vec{v}$, because very large values for the flux away from the real axis obscured the more interesting (and much smaller) values near this axis. For the same six time steps used in Figure 2, Figure 3 shows the momentum field superimposed upon contour maps of $\log_{10}|\psi|$. (In order not to lose detail near the real axis, *scaled momentum vectors* were plotted: if the magnitude of the momentum vector was greater than 1.5 times the average momentum for vectors within the viewing window, then the length of the momentum vector was reset to 1.5 times the average value).

The initial momentum distribution and amplitude are shown in part (a). These momentum vectors swirl counterclockwise around the point $z_{pp} = (6,0.493)$ (which lies just above the top edge of the figure). This *pinch point*[20] is the saddle point for the initial density in the complex plane and occurs at the distance $y_{pp} = k_0/(2\beta)$ above the center of the initial wave packet on the real axis. In addition, the length of the momentum vectors increases with the radial distance from this point. In part (b), for $t = 300$, the leading edge of the wave packet encounters the lower part of the barrier potential near $y = -0.3$. Momentum vectors in this region (and in the entire leading edge of the wave packet) are directed upward. In contrast, momentum vectors on the trailing edge of the wave packet are directed down toward negative values of y. An interesting feature shown by the amplitude contours is the tilt of the vertical axis, with the result that amplitude below

Propagation on a Grid

J. Chem. Theory Comput., Vol. 5, No. 3, 2009 **447**
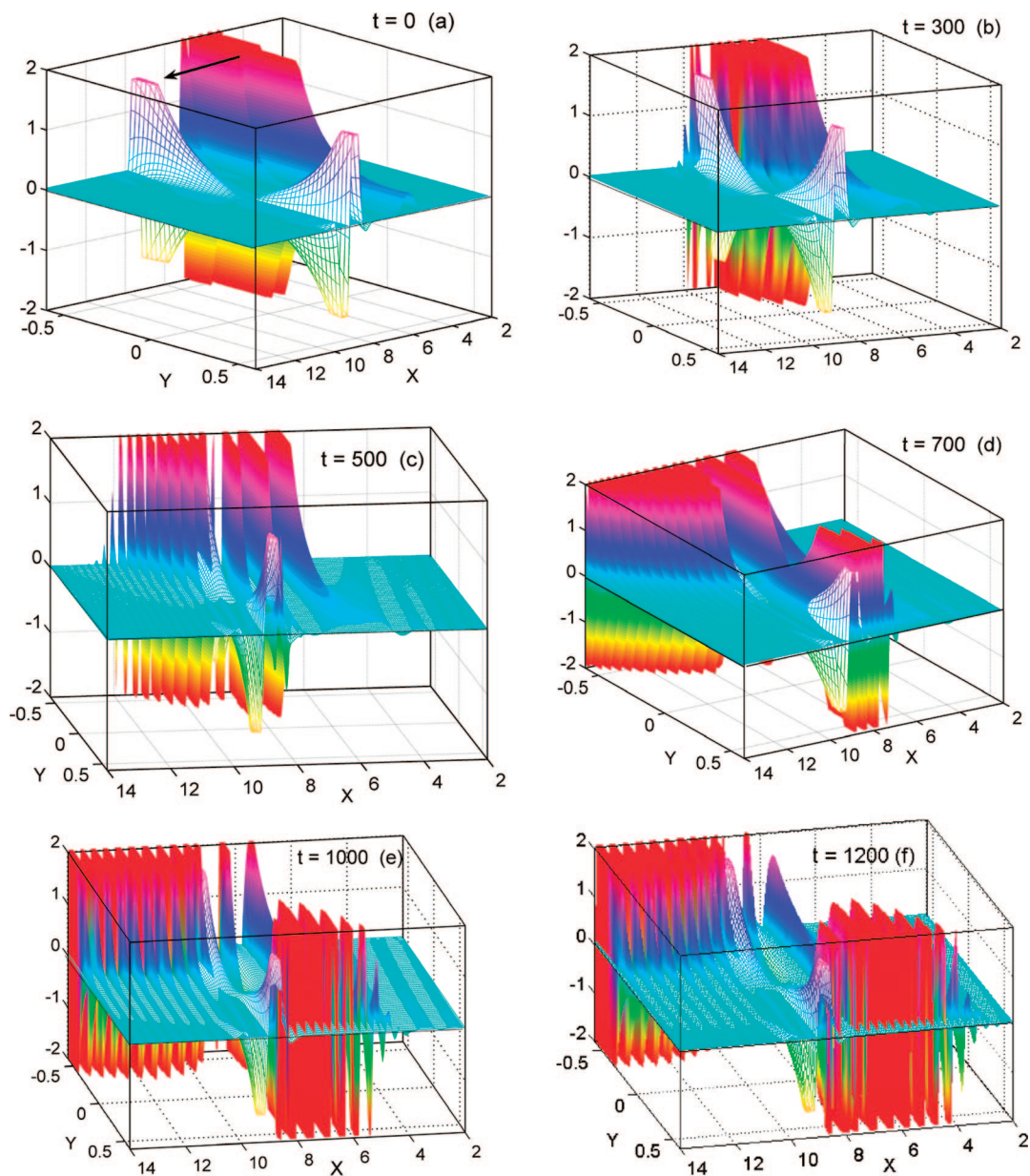
Figure 2. Time dependence of the real part of the scattering wave function. The initial wave packet energy is $E = V_0/4$. In each figure, a mesh plot of the imaginary part of the scaled complex Gaussian potential is also shown (see the caption to Figure 1). For these viewing angles, the initial wave packet moves from right to left, and the transmitted region is on the left-side of the figure.

the real axis encounters the barrier region before the upper component. In part (c), for $t = 500$, the leading edge of the packet for $y < 0.1$ has penetrated the lower part of the barrier region. In addition, the first of a series of ripples or undulations is developing near $y = 0.35$ and $x = 8.2$ on the reflected side of the barrier. These ripples form (for $400 < t < 700$) when amplitude that is thrust upward between $x = 8$ and $x = 9$ interferes with amplitude moving forward for $y > 0.3$. Starting with part (d), for $t = 700$, several ripples are noted above the real axis between $y = 0.1$ and $y = 0.3$. As seen in parts (e) and (f), for $t = 1000$ and $t = 1200$, respectively, these ripples (featuring five local maxima) gradually move down toward negative values of y, and the momentum vectors deflect (see the discussion below) around quasi-nodes in the amplitude.

When these ripples pass near the real axis, five relatively large oscillations are observed in the density along this axis. However, an observer confined to this axis would not sense the *vertical component* of the flow around the local minima as they form and decay. An additional feature shown in parts (e) and (f) is the 'fracture' of the wave packet near the barrier region. Although the momentum vectors for the transmitted packet have large components parallel to the real axis, those on the reflected side of the barrier form a much more complex pattern characterized by alternating regions with the flow directed either up or down in the y direction.

A blowup of the central portion of Figure 3(e), shown in Figure 4(a), displays counterclockwise circulation of the momentum vectors around four local maxima in the ampli-
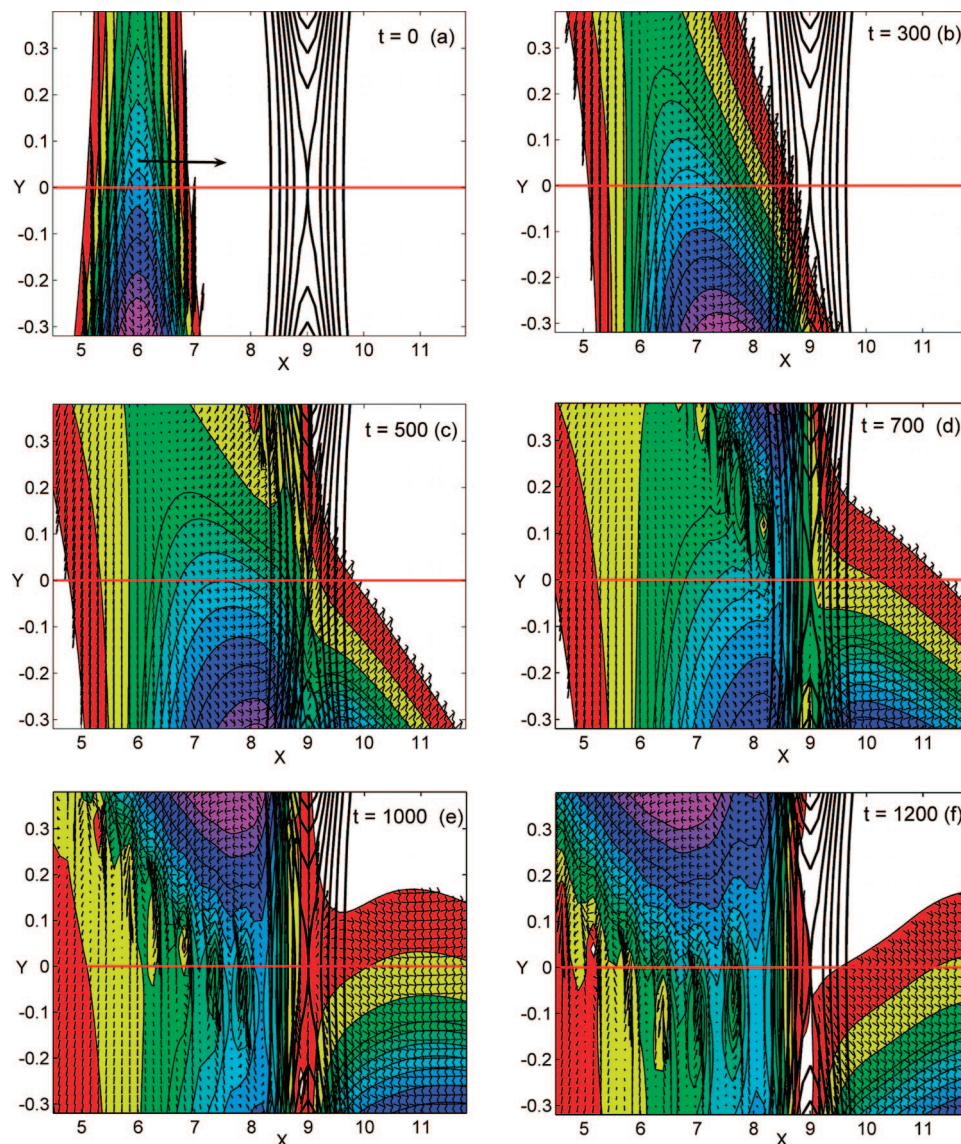
Figure 3. Time dependence of the quantum momentum (arrows) superimposed upon contour maps of log $_{10}|\psi|$. The initial wave packet energy is $E = V_0/4$. The *lower component* of the initial wave packet in (a) moves toward the right. The real axis is shown by the horizontal red line. Contours of the complex Gaussian potential energy are shown by the black contours. The 11 contour values for log $_{10}|\psi|$ are given by the following: $-2, -1.3, -0.8, -0.4, -0.25, -0.1, 0.05, 0.25, 0.45, 0.7, 0.9$.

tude. The momentum vectors have very small magnitudes near the local maxima, which are transient *stagnation points*. As time proceeds, these maxima gradually move toward the lower left of the figure, i.e., toward smaller values of x and negative values of y. On the real axis, local peaks in the amplitude for the reflected wave packet are approximately equally spaced and occur near the positions $x = 6.6, 7.1, 7.65$, and 8.2. At each of these positions, the momentum vectors have large components toward the left, in accord with the wave packet undergoing reflection from the barrier.

It is shown elsewhere[21] that the QMF near a stagnation point (z_s) may be approximately written $p(z,t) = p'(z_s,t)(z-z_s)$, where the spatial derivative is $p'(z,t) = \partial p(z,t)/\partial z$. If a test particle of mass m is launched from the position z_0, then it will follow the trajectory $z(t) = z_s + [z_0 - z_s] \exp[(p'(z_s,t)/m)t]$. It is useful to express $p'(z,t)$ in terms of real and imaginary parts: $p' = \alpha + i\beta$. For the case where $\alpha = 0$ and $\beta > 0$, the particle will trace out a counterclockwise orbit in

the complex plane. This is the situation pertaining to the momentum field shown in Figure 4(a). Other categories of orbits (for various values of α and β) near a stagnation point have been described.[21]

Between the four local maxima in Figure 4(a) are three quasi-nodes (the approximately circular yellow regions). In two or more *real* coordinates, quantum momentum vectors form approximately *circular paths* around nodes in the wave function. The circulation integral around these closed paths is quantized in integer multiples of $2\pi\hbar$. Bearing this in mind, it may be surprising that the momentum vectors in Figure 4(a) do *not* show circular flow around these local minima. Rather, the flow follows four *hyperbolic paths*: directed up on the left-side, down on the right-side, horizontal toward the left above the minimum, and horizontal toward the right below the minimum. In the following section, this flow will be analyzed in terms of another vector field.

Propagation on a Grid

J. Chem. Theory Comput., Vol. 5, No. 3, 2009 **449**
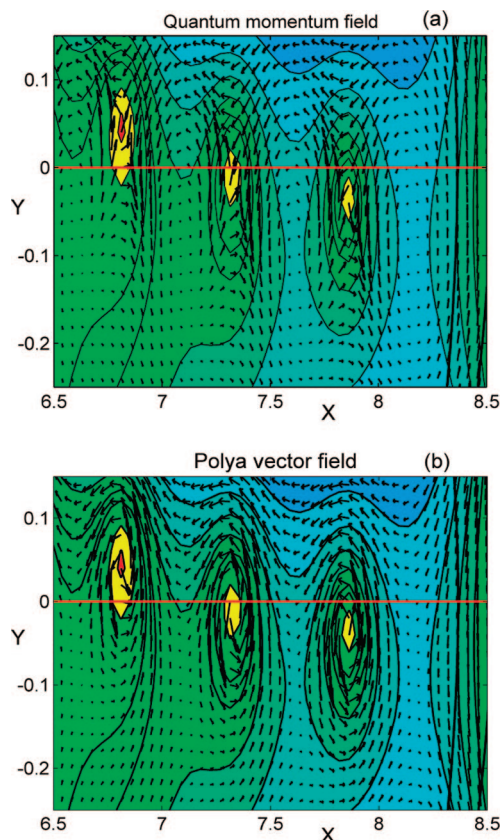
Figure 4. (a) Quantum momentum field (arrows) superimposed upon a contour map of $\log_{10}|\psi|$ for $t = 1000$. This figure, which shows hyperbolic flow around three quasi-nodes, is a blowup of the central region of Figure 3(e). The real axis is shown by the red line. Several contours (in black) of the complex Gaussian potential energy are shown on the right side of the figure. (b) Pólya vector field associated with this momentum field, showing counterclockwise circular flow around the three quasi-nodes.

6. The Pólya Vector Field and Vorticity

In order to analyze hyperbolic flow, the QMF for a model wave function will be plotted. For the function $\phi(z) = (z - z_0) \exp(-\beta(z - z_0)^2)$, which has a node at z_0, the QMF is given by

$$p(z) = \frac{\hbar}{i}\left[\frac{1}{z - z_0} - 2\beta(z - z_0)\right] \qquad (12)$$

This function has a first order pole at z_0. The vector map for $p(z)$ is shown in Figure 5(a). (Similar plots appear in *Visual Complex Analysis*:[39] see Figures 1 and 5 in Chapter 10.) Near the node, two diagonal separatrices confine the flow within four quadrants. Because of this confinement, momentum vectors cannot circulate completely around the node. Within each quadrant, the flow is directed inward near one separatrix and outward along the other. Quantum trajectories (which are tangent to the streamlines) are forced away from the nodal point by the quantum force, the gradient of the quantum potential. Using the first term in eq 12, the quantum force near the node is given by[40]

$$F_q(z) = -\frac{\hbar}{2mi}\frac{\partial^2 p}{\partial z^2} = \frac{\hbar^2}{m}\frac{1}{(z - z_0)^3} = \frac{\hbar^2}{m}\frac{1}{r^3}e^{-3i\theta} \qquad (13)$$
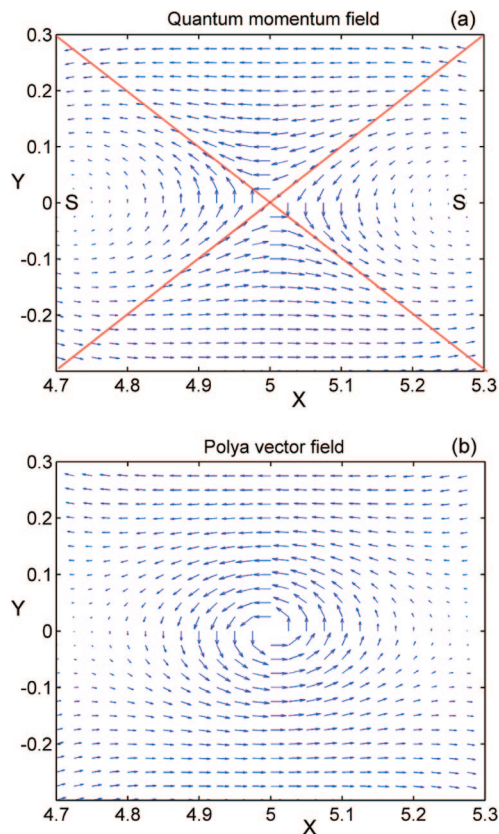
Figure 5. Quantum momentum field near a node in a model wave function is shown in part (a). This wave function has a node at the middle of the figure. In-flow and out-flow asymptotes (separatrices) are shown by the two (red) diagonal lines. Two stagnation points (S) are shown on the left and right edges of the figure. Part (b) shows the associated Pólya vector field. This field shows counterclockwise circular flow around the nodal point.

where $z = z_0 + r \exp(i\theta)$ was used in the last step. The vector map of this function (not shown here) clearly shows the r^{-3} repulsive character near the node (except along the asymptote at $\theta = \pi/4$.)

An alternative way of describing and visualizing flow in the complex plane will now be introduced. This function was utilized previously[40] in an analysis of quantum vorticity in the complex plane. We begin by considering the circulation integral: the line integral of the QMF around a simple closed curve in the complex plane. According to the Cauchy integral theorem,[38] this integral vanishes if $p(z)$ is analytic on and within the bounding contour. If both the line element and the QMF in the circulation integral are decomposed into real and imaginary parts, we obtain[38,39] (the momentum vector has the components $\vec{p}(z) = [p_r, p_i]$)

$$\oint p(z)dz = \oint (p_r + ip_i)(dx + idy)$$

$$= \oint (p_r dx - p_i dy) + i\oint (p_r dy + p_i dx)$$
$$= \oint \vec{P} \cdot d\vec{t} + i\oint \vec{P} \cdot d\vec{n} \qquad (14)$$

In the last step, the Pólya vector field has been introduced;[38,39] this vector is defined by $\vec{p} = [p_r, -p_i]$ or as a complex function, $P(z,t) = p^*(z,t)$. In addition, the tangent along the integration contour and the outward normal vector along the
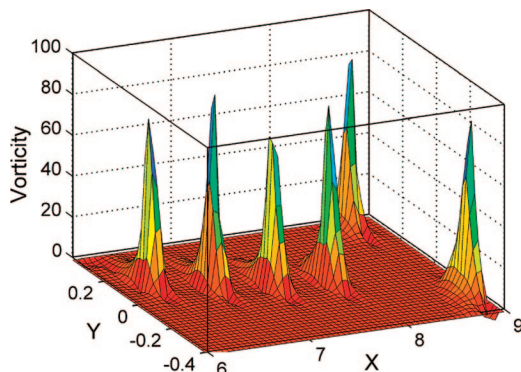
Figure 6. Vorticity field for time $t = 1000$. The four peaks for $x < 8$ form at the positions of the four peaks in $imag(S(z,t))$ shown in Figure 7(a).

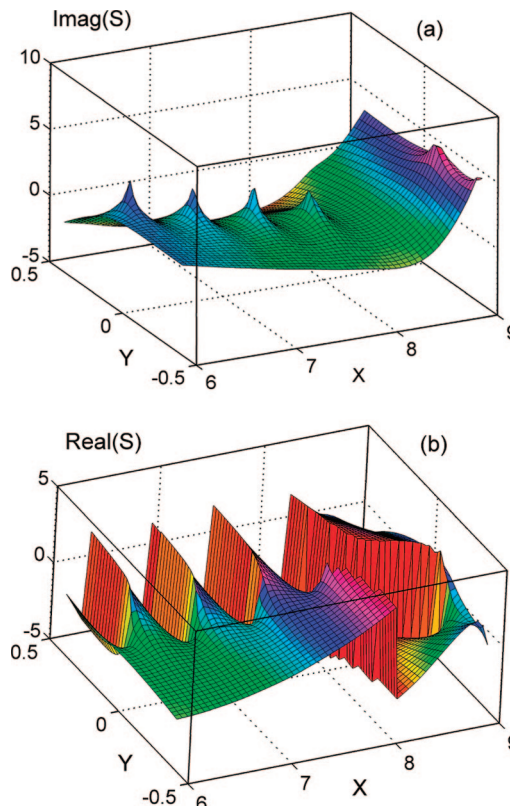**Figure 7.** The imaginary (a) and real (b) parts of the complex quantum action function for the time $t = 1000$. In part (b), the principal value of the multivalued function is shown. These figures should be compared with the amplitude and QMF plotted in Figure 3(e) and the QMF and Pólya vector fields plotted in Figure 4.

integration contour are $dt^{\rightarrow} = [dx, dy]$ and $dn^{\rightarrow} = [dy, -dx]$, respectively.

Although the Pólya field contains the same information as the momentum field, this information is displayed differently. To continue with the example mentioned previously, Figure 5(b) shows the Pólya field corresponding to the QMF plotted in part (a) of this figure. The vectors plotted in this figure clearly show counterclockwise circular flow around the nodal point. In this case, if the integration contour encloses the pole in $p(z)$, the imaginary term in the last step of eq 14 vanishes and the circulation integral is real-valued (and takes the value $2\pi\hbar$, corresponding to a quantized vortex in the 'ground state'). Returning to the reflected wave packet for the barrier scattering problem, Figure 4(b) shows the Pólya field corresponding to the QMF in part (a). The Póla field, as expected, shows counterclockwise circular flow around each of the three quasi-nodes. There are two additional features evident from this figure: (a) the Pólya vectors are always tangent to contours of the wave function amplitude (or the density); (b) the Pólya vectors display hyperbolic flow around stagnation points, such as the local maxima in the amplitude shown in this figure. The first property is generally valid for any wave function.[40] It has also been shown that Pólya vectors are parallel to contours of $imag(S)$ and orthogonal to contours of $real(S)$, where $S(z,t)$ is the complex action function.[40] The complex action function is considered further in the next section.

The local circulation of a vector field is frequently measured by the vorticity, the curl of the field. Accordingly, the vorticity of the Pólya field is given by

$$\vec{\Omega}(z,t) = \vec{\nabla} \times \vec{P}(z,t) = \frac{\partial P_i}{\partial x} - \frac{\partial P_r}{\partial y} \quad (15)$$

In regions where the field is analytic, the vorticity is zero, so that the magnitude of the vorticity vector may be viewed as a local measure of nonanalyticity. The vorticity is plotted in Figure 6 for $t = 1000$. The four sharp peaks for $x < 8$ form at the positions of the four quasi-nodes in the wave function (and at the four peaks in $imag(S(z,t))$ shown in Figure 7(a)). These peaks gradually move to the left toward small values of x as the packet reflects from the barrier. There are also two peaks close to the barrier maximum, at $x_b = 9$, and these gradually decay as the wave packet bifurcates.

7. The Complex Action

The complex action function, $S(z,t)$, not only determines the wave function through the exponential ansatz, $\psi(z,t) = \exp[iS(z,t)/\hbar]$, but also displays interesting features that will be illustrated in this section. If this function is decomposed into real and imaginary parts, $S = S_r + iS_i$, the wave function then becomes $\psi(z,t) = \exp[-S_i(z,t)/\hbar] \exp[iS_r(z,t)/\hbar]$. From this expression, it is evident that the imaginary part of the action determines the amplitude of the wave function. Large positive values of S_i imply small values for the amplitude. In addition, the real part of the action, the 'pure phase', also has interesting properties, which will now be considered.

For the barrier scattering example, Figure 7(a) shows the imaginary part of $S(z,t)$, while part (b) shows the real part of this function. In part (a), the four peaks in $imag(S(z,t))$ between $x = 6$ and $x = 8$ are associated with the four quasi-nodes evident in Figures 3(e) and 4. Part (b) shows the principal zone of the phase, with values in the range $-\pi \leq real(S(z,t)) \leq \pi$. Starting near the position of each quasi-node and progressing in the positive y direction are sharp discontinuities of 2π in the phase. Discontinuities of this type are expected near nodes or quasi-nodes. For example, the model wave function $\phi(z) = z \exp(-\beta z^2 - iKz)$ has a QMF displaying hyperbolic flow near $z = 0$ and a phase discontinuity in $real(S(z,t))$ along the positive y direction. For $\phi(z)$, the action function is given by $S(z) = -i\hbar[\ln(z) - \beta z^2 - iKz]$. It is important to note that the complex function $\ln(z)$

Propagation on a Grid

J. Chem. Theory Comput., Vol. 5, No. 3, 2009 **451**

is multivalued: $\ln(z) = \ln|z| + iArg(z) + 2m\pi i$, where the principal zone of the argument is $\pi \le Arg(z) \le \pi$, and $m = 0, \pm1, \pm2,...$ As a result, the action function is also multivalued. When the principal sheet, corresponding to $m = 0$, and the sheets for $m = \pm1, \pm2,...$ are plotted, the Riemann surface for this function is obtained.

8. Summary

The time-dependent scattering of a wave packet from a Gaussian barrier was computationally investigated in the complex plane. Time evolution of the wave packet was followed by plotting the real part of the wave function and the quantum momentum field. In the reflected packet, an important role was played by ripples forming *above* the real axis. When these ripples pass near the real axis, 'interference fringes' are observed in the density. However, an observer confined to this axis would be ignorant of the significant vertical component of the flow (along the imaginary axis) near the local maxima and minima. In contrast, the component of the packet *below* the real axis makes a significant contribution to the transmitted packet. The quantum momentum vector maps show hyperbolic flow forming four 'petals' around transient quasi-nodes in the amplitude and counterclockwise circular flow around stagnation points, including local maxima in the amplitude. When the Pólya vector field associated with this momentum field was plotted, circular counterclockwise flow was obtained around the quasi-nodes. The vorticity, the curl of the Pólya field, is used to pinpoint regions of nonanalyticity in the QMF. These are also the positions where peaks occur in the imaginary part of the quantum action function.

Wave packet dynamics in the complex plane has been studied through an alternate approach: *numerical analytic continuation* from the wave function computed directly on the real axis.[45] Fortunately, within the viewing window, $\psi(z,t)$ turns out to be in excellent agreement with the results described in the current study.

References

(1) Thaler, B. *Visual Quantum Mechanics*; Springer-Verlag: New York, 2000.

(2) Kemble, E. C. *Phys. Rev.* **1935**, *48*, 549.

(3) Berry, M. V.; Mount, K. E. *Rep. Prog. Phys.* **1972**, *35*, 315.

(4) Stine, J.; Marcus, R. A. *Chem. Phys. Lett.* **1972**, *15*, 536.

(5) Miller, W. H.; George, T. F. *J. Chem. Phys.* **1972**, *5668*, 56.

(6) George, T. F.; Miller, W. H. *J. Chem. Phys.* **1972**, *57*, 2458.

(7) Doll, J. D.; George, T. F.; Miller, W. H. *J. Chem. Phys.* **1973**, *58*, 1343.

(8) Miller, W. H. *Adv. Chem. Phys.* **1974**, *25*, 69. 1974.

(9) Huber, D.; Heller, E. J. *J. Chem. Phys.* **1987**, *87*, 5302.

(10) Heller, E. J. *J. Chem. Phys.* **1975**, *62*, 1544.

(11) Boiron, M.; Lombardi, M. *J. Chem. Phys.* **1998**, *108*, 3431.

(12) Tannor, D. J. *Introduction to Quantum Mechanics: A Time Dependent Perspective*; University Science Books: Sausalito, CA, 2007.

(13) John, M. V. *Found. Phys. Lett.* **2002**, *15*, 329.

(14) Yang, C. D. *Chaos, Solitons Fractals* **2006**, *30*, 342.

(15) Yang, C. D. *Chaos, Solitons Fractals* **2006**, *32*, 312.

(16) Yang, C. D. *Annal. Phys.* **2005**, *319*, 399.

(17) Yang, C. D. *Int. J. Quantum Chem.* **2006**, *106*, 1620.

(18) Yang, C. D. *Annal. Phys.* **2005**, *319*, 444.

(19) Yang, C. D. *Chaos, Solitons Fractals* **2006**, *30*, 41.

(20) Chou, C. C.; Wyatt, R. E. *Phys. Rev. A* **2006**, *76*, 012115.

(21) Chou, C. C.; Wyatt, R. E. *J. Chem. Phys.* **2008**, *129*, 124113.

(22) Sanz, A. S.; Miret-Artés, S. *Chem. Phys. Lett.* **2008**, *458*, 239.

(23) Lopreore, C. L.; Wyatt, R. E. *Phys. Rev. Lett.* **1999**, *82*, 5190.

(24) Wyatt, R. E. *Quantum Dynamics with Trajectories*; Springer: New York, 2005.

(25) Trahan, C. J.; Hughes, K.; Wyatt, R. E. *J. Chem. Phys.* **2003**, *118*, 9911.

(26) Trahan, C. J.; Wyatt, R. E. *J. Chem. Phys.* **2003**, *119*, 7017.

(27) Trahan, C. J.; Wyatt, R. E. *Chem. Phys. Lett.* **2004**, *385*, 280.

(28) Hughes, K. *J. Chem. Phys.* **2005**, *122*, 11.

(29) Bittner, E. R. *J. Chem. Phys.* **2004**, *119*, 1358.

(30) Trahan, C. J.; Wyatt, R. E.; Poirier, B. *J. Chem. Phys.* **2005**, *122*, 164104.

(31) Rowland, B. A.; Wyatt, R. E. *Chem. Phys. Lett.* **2006**, *426*, 209.

(32) Goldfarb, Y.; Degani, I.; Tannor, D. J. *J. Chem. Phys.* **2006**, *125*, 231103.

(33) Rowland, B. A.; Wyatt, R. E. *J. Phys. Chem. A* **2007**, *111*, 10234.

(34) Sanz, A. S.; Miret-Artés, S. *J. Chem. Phys.* **2007**, *127*, 197101.

(35) Goldfarb, Y.; Degani, I.; Tannor, D. J. *J. Chem. Phys.* **2007**, *127*, 197102.

(36) Goldfarb, Y.; Schiff, J.; Tannor, D. J. *J. Phys. Chem. A* **2007**, *111*, 10416.

(37) Goldfarb, Y.; Tannor, D. J. *J. Chem. Phys.* **2007**, *127*, 161101.

(38) Pólya, G.; Latta, G. *Complex Variables*; Wiley: New York, 1974.

(39) Needham, T. *Visual Complex Analysis*; Oxford University Press: Oxford, 1997.

(40) Chou, C. C.; Wyatt, R. E. To be published.

(41) Zhang, J. Z. H. *Theory and Application of Quantum Molecular Dynamics*; World Scientific: Singapore, 1999.

(42) Vibok, A.; Balint Kurti, G. G. *J. Phys. Chem.* **1992**, *96*, 8712.

(43) Press, W. H.; Teukolsky, S. A.; Vetterling, W. T.; Flannery, B. P. *Numerical Recipes;* Cambridge University Press: New York, 1992.

(44) Verlet, L. *Phys. Rev.* **1967**, *159*, 98.

(45) Rowland, B. A.; Wyatt, R. E. To be published.